Journal of the Optical Society of America A
OPTICS, IMAGE SCIENCE, AND VISION

Investigation of the anisotropy and scaling of the phase structure function of a spatially coherent light beam propagating through convective air turbulence

Saifollah Rasouli,[1,2,3,*] Ebrahim Mohammadi Razi,[1,4] and J. J. Niemela[3]

[1]Department of Physics, Institute for Advanced Studies in Basic Sciences (IASBS), Zanjan 45137-66731, Iran
[2]Optics Research Center, Institute for Advanced Studies in Basic Sciences (IASBS), Zanjan 45137-66731, Iran
[3]The Abdus Salam ICTP, Strada Costiera 11, 34151 Trieste, Italy
[4]Faculty of Physics, Department of Basic Sciences, University of Bojnord, 1339 Bojnord, Iran
*Corresponding author: rasouli@iasbs.ac.ir

Received 23 May 2022; revised 12 July 2022; accepted 24 July 2022; posted 25 July 2022; published 18 August 2022

We report on applications of moiré deflectometry in measurements of the anisotropy and scaling of the phase structure function (PSF), obtained after passing a laser beam through an indoor enclosure containing convective air turbulence. We combine the use of two telescopes, with a two-channel wavefront sensor based on moiré deflectometry, to attain high sensitivity and resolution to fluctuations in the wavefront phase, caused by turbulent fluctuations in the enclosure. The measurements of the wavefront PSF along two directions perpendicular to the direction of the light beam propagation at different heater temperatures show that the convective air turbulence is anisotropic turbulence, where the value of the anisotropy increases with increasing temperature gradient. Various models are fitted to the measured PSFs, and we find that the turbulent is also non-Kolmogorov, in which, for the separation distances of two points on the wavefront less than 10 cm, the von Kármán PSF is the best fit to the experimental data. For higher values of separations, the experimental data do not fit with existing models. By fitting the von Kármán PSF on the data, we estimate values of the refractive index structure constant, C_n^2, as well as the outer scale of the turbulence. The value of the outer scale decreases with increasing temperature of the heater up to approximately 50°C, where it saturates, while the value of C_n^2 monotonically increases. Over the complete range of heater temperatures, from 40°C to 160°C, the Rayleigh number, Ra, for the enclosed air flow varied from $5.80 \times 10^8 < \mathrm{Ra} < 5.89 \times 10^9$ so that all measurements were conducted in a state of developed convective turbulence.

https://doi.org/10.1364/JOSAA.464285

1. INTRODUCTION

A complete understanding of turbulence remains elusive due to the complexity of the underlying equations of motion, as well as the inability of fully resolved direct numerical simulations to adequately follow turbulence at the intensity levels routinely found in large-scale natural or engineering flows [1]. For this reason, there has always been an exceptional need for guidance from experiments and, in turn, the development of novel methods of measuring the statistical properties of turbulent flows [2–4]. Various phenomenological models have been developed that describe quite well the main features of atmospheric turbulence, including the Kolmogorov, Tatarskii, and von Kármán models, differing in their specification of the inner and outer-scale parameters (the smallest and largest scales of turbulence, respectively) [5]. The von Kármán–Tatarskii model combines features of the latter two models and is sometimes called the modified von Kármán model. In all these models, it is proposed that the turbulence is isotropic and homogeneous; an approximation that we point out is rarely—if ever—completely satisfied in either nature or laboratory experiments. Experimental studies show that the statistics of wavefront phase propagation through the atmosphere, or in controlled laboratory confinement of turbulent flows, do not always precisely obey the power laws associated with the Kolmogorov model of turbulence [6–12], even under conditions and in the range of scales where one might expect homogeneity and isotropy to hold [13–23]. Thus, several models such as the Tatarskii, Greenwood, Pump, von Kármán, and modified von Kármán have been proposed to represent the statistical behavior of the turbulence phase fluctuations. Accordingly, Gudimetla *et al*. [24] derived an analytical expression for the long amplitude correlation function

for a plane wave propagating through an anisotropic non-Kolmogorov turbulent atmosphere. Toselli and Korotkova [25] introduced a model for a non-classic spatial power spectrum involving anisotropy along two mutually orthogonal axes transverse to the direction of the beam propagation. Yao *et al*. [26] investigated the effect of anisotropic non-Kolmogorov turbulence on the propagation of the stochastic electromagnetic beam. They also explored the outcome of an anisotropic parameter on the spectral density, spectral degree of coherence, and spectral degree of the polarization of the beam. Xiao *et al*. [27] extended the Gaussian beam theory for propagation through Kolmogorov turbulence to anisotropic turbulence along with horizontal directions. They also studied the effects of the different spectral slopes on beam propagation.

Much research has been done on the propagation of different wavefronts from non-Kolmogorov turbulence. Wanjun *et al*. [28] derived the average intensity of Bessel Gaussian beams propagating through non-Kolmogorov turbulence based on the Rytov theory. Ma *et al*. [29] derived an analytical expression for rectangular multi-Gaussian Schell-model array beams propagating through free space and non-Kolmogorov turbulence. Huang *et al*. [30] investigated the effect of anisotropic non-Kolmogorov turbulence on the evolution behavior of the average intensity and coherent vortices for Gaussian Schell-model vortex beams.

Although various effects of atmospheric and indoor convective turbulence on some features of the light beam propagating through them have been investigated [16,20,23,31–33], based on our knowledge, until now there have been no comprehensive studies on the effect of a two-dimensional (2D) temperature gradient on the statistical properties of the phase structure function (PSF) of a light beam wavefront after propagating through a turbulent medium. In the work presented below, we report on applications of a two-channel moiré deflectometry-based wavefront sensor for measuring the power-law scaling and anisotropy of the PSF corresponding to controlled laboratory convective air turbulence, in the presence of weak to strong 2D temperature gradients.

It is worth mentioning that in four other works the same sensor was used for investigating the wavefront distortions induced by atmospheric turbulence [12], the inhomogeneity of atmospheric turbulence at day and night times [18], the effects of the source temperature and its distance on the statistical behavior of the convective air turbulence [22], and the annular Zernike polynomials behavior in convective air turbulence in the presence of the 2D temperature gradient [23].

In comparison with a Shack–Hartmann wavefront sensor [34], the two-channel moiré deflectometry-based wavefront sensor used here is relatively low cost. For instance, the sensor gratings can be easily designed with simple computer software and can be printed on plastic paper with a commercial printer. This method also offers some flexibility, since its dynamic range and sensitivity are adjustable by merely changing the separation of the gratings and the angle between the rulings of the gratings in both channels, respectively. The spatial resolution of the wavefront sensing is also adjustable by means of bright, dark, and virtual traces for given moiré fringes with no cost in measurement precision. This sensor can even detect the presence of optical vortices on the wavefront that might be generated in a highly turbulent condition [35]. The main drawback of the moiré deflectometry-based wavefront sensor is the need for a high-level intensity beam, and, therefore, for low light applications as one would normally expect in astronomy, highly sensitive detectors are required. However, to decrease the energy loss, moiré deflectometers can be setup with phase gratings.

2. GOVERNING EQUATIONS

The phase variance between two separate points on the wavefront is defined as the PSF and is given by [36]

$$D_\phi(\xi) = \left\langle |\phi(r) - \phi(r+\xi)|^2 \right\rangle, \tag{1}$$

where ϕ is the wavefront phase, ξ is the separation distance between two points on the wavefront, and $\langle ... \rangle$ represents an ensemble average. Fried has shown that the PSF in the Kolmogorov model of atmospheric turbulence is given by [36]

$$D_\phi(\xi) = 6.88\left(\frac{\xi}{r_0}\right)^{5/3}, \tag{2}$$

where r_0 is Fried's seeing parameter, and $l_0 < \xi < L_0$, where L_0 and l_0 are the outer and inner-scale parameters, respectively.

The anisotropic nature of turbulence can be taken into account by modifying the PSF, leading to [37]

$$D_\phi(u) = \gamma_{\beta_u}\left(\frac{u}{\rho_{0u}}\right)^{\beta_u - 2}, \quad u = x, y, \tag{3}$$

where β_u, γ_{β_u}, and ρ_{0u} are, respectively, the exponent of the power spectrum for the index of refraction fluctuations, the function of the power spectrum exponent, and the generalized Fried's "seeing" parameter in the horizontal and vertical directions.

In this work, we have measured $D_\phi(x)$ by observing the difference of phase between pairs of points, with a given value of separation in the horizontal direction, x, displaced spatially on the reconstructed wavefront on the second telescope aperture. We have done these calculations for all of the successive reconstructed wavefronts. Now, by repeating the process for other possible values of x, $D_\phi(x)$ can be determined as a function of x. A similar process is used for measuring $D_\phi(y)$, where y is the separation in the vertical direction.

3. EXPERIMENTAL WORKS AND RESULTS

A schematic diagram of the experimental setup is shown in Fig. 1. In the experiment, the second harmonic of a CW diode pumped $Nd-Y_3Al_5O_{12}$ (YAG) laser beam with a wavelength of 532 nm enters the first telescope (a 14 in. Celestron Schmidt-Cassegrain telescope) and is expanded to a diameter of 20 cm and recollimated by it before passing horizontally through an enclosure of convectively turbulent air, formed by imposing a vertical temperature (density) gradient. For this purpose, we used a flat plane heater with an upper surface area of 50 cm × 100 cm. The temperature at the heater was controlled and was varied in a range from 28°C to 160°C with a step of 10°C. In steady-state condition, the temperature fluctuations were less than 1°C. We want to point out that under steady-state

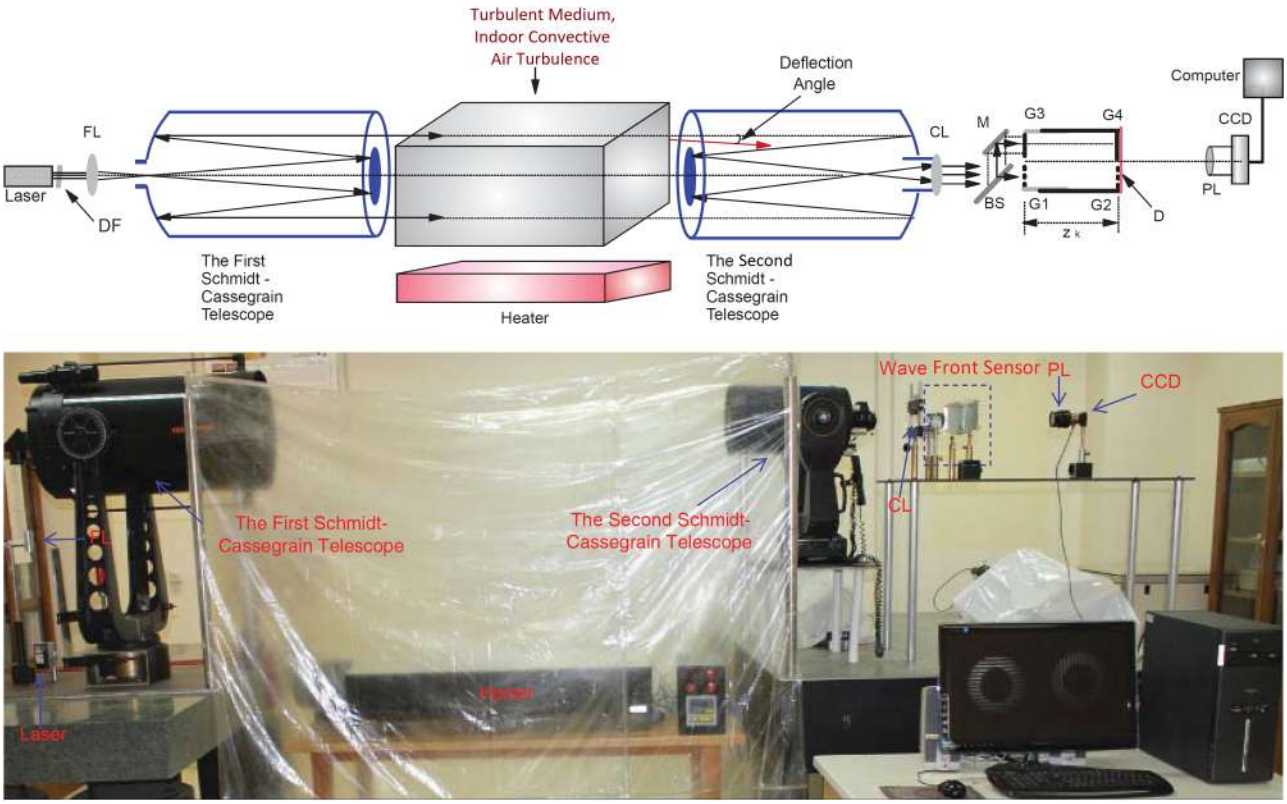

Fig. 1. Top: schematic diagram of the experimental setup. Bottom: integrated instrument. DF, FL, CL, BS, M, D, and PL denote the neutral density filter, focusing lens, collimating lens, beam splitter, mirror, diffuser, and projecting lens, respectively. $G1$, $G2$, $G3$, and $G4$ stand for the gratings.

conditions a horizontal component of the temperature gradient appeared due to the finite width of the heater's surface. A set of digital thermometers were used to measure the temperature gradients [23]. According to the data collected by the thermometers, the temperature gradients in the vertical and horizontal directions were not equal. The temperature and temperature gradient fluctuations for the same turbulent medium can be found in Figs. 2 and 3 of Ref. [23]. The height of telescopes from the plane of the heater was 80 cm.

The intensity of the turbulence was determined from the Rayleigh number Ra defined as

$$\mathrm{Ra} = \frac{g\beta(T_s - T_\infty)\ell^3}{\nu\alpha}, \tag{4}$$

where g is the acceleration of gravity, β is the isobaric thermal expansion coefficient of air, T_s and T_∞, respectively, are the temperature at the heater surface and the flow at a height $\ell = 80$ cm above it, ν is the kinematic viscosity, and α is the thermal diffusivity of the air. For different measurements, the mean temperature values at the heater surface and path of the laser beam having a height $\ell = 80$ cm from the heater and the corresponding Rayleigh numbers are reported in Table 1. For the heater temperatures considered in this study, the Rayleigh number is in the range of $5.80 \times 10^8 < \mathrm{Ra} < 5.89 \times 10^9$, which is in the developed turbulent regime [38].

The length of the heater was parallel to the path of the laser beam. After passing through the turbulent area, the beam enters the second telescope's aperture (a Meade 8 in. LX200 GPS Schmidt-Cassegrain telescope), separated from the first telescope by 150 cm.

Table 1. Rayleigh Number of the Convective Air Turbulence

T_s (°C)	T_∞ (°C)	Ra	T_s (°C)	T_∞ (°C)	Ra
40	29.2	5.80×10^8	110	32.3	3.75×10^9
50	29.6	1.05×10^9	120	32.5	4.19×10^9
60	30.3	1.51×10^9	130	32.6	4.64×10^9
70	30.5	1.97×10^9	140	33.4	5.04×10^9
80	31.5	2.4×10^9	150	33.6	5.47×10^9
90	31.7	2.86×10^9	160	33.9	5.89×10^9
100	32.2	3.29×10^9			

The beam was subsequently collimated by a positive lens and passed through a beam splitter and a pair of moiré deflectometers installed parallel and close together. Directions of the grating rulings were almost parallel in each moiré deflectometer but were perpendicular in the two channels. The grating holders were held on rotary mounts, which could be rotated about the optical axis to adjust the angle between the grating rulings. In the experimental setup shown in Fig. 1, G2 and G4 were installed at a distance of 37.5 cm from G1 and G3, respectively. All the gratings were identical and had a ruling period of 0.1 mm. For different turbulent strengths, we considered an angle of 4.2° between the grating rulings in both moiré deflectometers. For this case, the number of the moiré fringes was about 15 (as seen in Fig. 2). Moiré patterns were formed on a plane where the second grating of the moiré deflectometers and a diffuser were

installed. The moiré patterns from both channels are projected onto a CCD camera. For a displacement of the self-image in a direction normal to the grating rulings, moiré fringes were shifted in a direction normal to the moiré fringe direction [39]. It is worth mentioning that the scattering effect of the diffuser helps us image exactly the plane of the second gratings of the moiré deflectometers (where the moiré patterns formed) on the CCD's sensitive area. The deformation of the moiré fringes caused by the turbulence can be measured by tracing the imaged moiré fringes. The laser beam intensity was reduced by a neutral density filter to a level below the saturation level of the CCD. Successive moiré patterns are recorded by the CCD camera (model DCC1545M, high-resolution USB2.0 CMOS camera, Monochrome) and transferred to a computer to allow temporal fluctuations of the wavefront phase to be measured with high accuracy. The sampling rate was 30 frames/s, and the exposure time for a frame was 1 ms. Displacements of the moiré fringes in the recorded patterns correspond to the fluctuations of two orthogonal components of the angle of arrival (AA) across the wavefront. Since the AA components, α_x and α_y, are equal to the incident wavefront gradients in the x and y directions, respectively, the incident wavefront gradients at a given point are determined by [39]

$$[\alpha_x, \alpha_y] = \frac{f'}{f}\frac{d}{z_k}\left(\frac{\Delta x_m}{d_m} + \frac{\Delta y_m}{d'_m}\right), \tag{5}$$

where f is the second telescope's focal length, f' is the focal length of the collimating lens, d is the gratings' ruling period, z_k is the gratings' distance, d_m is the moiré fringes spacing, and Δy_m and Δx_m are the moiré fringe shifts in the first and second channels, respectively. As is seen from Eq. (5), by increasing the gratings' distance, decreasing the period of the gratings d, or increasing the moiré fringe spacing d_m, the measurement precision of AA fluctuations can be improved. Another improving factor is f'/f, which appears due to the use of the telescope. Since the moiré fringe spacing d_m is given by $\frac{d}{2\sin(\theta/2)}$, it can be easily changed by changing the angle between the gratings' rulings θ. A change in the value of θ, however, affects the value of d_m, and this in turn affects the spatial resolution of the measurements.

In the current research, we have used $d = 0.1$ mm, $f = 200$ cm, $f' = 20$ cm, and $z_k = 37.5$ mm. The moiré pattern in each channel consists of about 404 pixels × 404 pixels, and d_m was covered by 26 pixels in both channels. By considering that the minimum measurable displacement of a fringe trace in the CCD's plane within sub-pixel accuracy is $\delta y_{m_{\min}} = \delta x_{m_{\min}} = 1$ pixel/10 [39], the minimum measurable AA fluctuation is 1.02×10^{-6} rad or 0.21 arc s.

On the other hand, if we assume that the maximum measurable displacement of a trace is equal to half the moiré fringe spacing, $(\frac{\Delta x_m}{d_m})_{\min} = (\frac{\Delta y_m}{d'_m})_{\min} = \frac{1}{2}$, according to Eq. (5), AA fluctuations in the range of $-\frac{1}{2}\frac{f'}{f}\frac{d}{z_k}$ to $+\frac{1}{2}\frac{f'}{f}\frac{d}{z_k}$ would be measured. Thus, for the above-mentioned values of the experimental parameters, one can measure AA fluctuations in the range of −27 to +27 arcsec without making any adjustment in the setup.

The traces of the bright and dark vertical and horizontal moiré fringes and first-order virtual traces were derived from about 15 moiré fringes shown in each channel of the wavefront sensor. The traces of points with intensities equal to the mean intensity of the adjacent bright and dark traces are the so called the first-order virtual traces [39]. In a moiré pattern, there are 15 bright moiré fringes, and between any two of them there is a dark moiré fringe. We also consider position of the mean intensities between two adjacent bright and dark moiré fringes as a first-order virtual trace. Therefore, the number of virtual fringes is 28. Now, in either the vertical or horizontal direction, we have 57 traces, and, in two directions, their intersection points can form an array of maximum 55 × 55 points. In practice, we do not have access to some of the intersection points because they correspond to the central area and corners of the moiré patterns. It is worth noting that the spatial resolution of the phase measurements is limited by the number of moiré fringes covering the full aperture of the second telescope and the number of virtual moiré fringes between two adjacent moiré fringes. By observing the fluctuations in successive frames, the evolution of the wavefront shape was determined. At given temperature of the heater, we have recorded at least five sets of data. Each set of data was collected in 66 s and contained 2000 frames. In these experiments, 1677 intersection points of the 15 bright and 14 dark moiré fringes and 28 first-order virtual fringes were used for wavefront reconstruction. The distance between two adjacent intersection points corresponds to 3.1 mm in real space on the second telescope's aperture plane. Three typical recorded frames at three different values of the heater temperature, as well as their corresponding reconstructed wavefront surface plots, are shown in Fig. 2. The background movie of Fig. 2 contains 300 successive recorded frames and corresponding plots of the reconstructed wavefront surface (Visualization 1). Since the wavefront slopes were determined exactly on the intersection points, using the Southwell numerical integration method and the zonal wavefront reconstruction algorithm, we have reconstructed the wavefront phase [40,41]. See [12,23,39] for more details on the wavefront surface reconstruction. A similar method was used for studying the dynamic behavior of thermal distortions of the wavefront in a high-power thin-disk laser [42].

Figure 3 shows values of $D_\phi(x)$ and $D_\phi(y)$ calculated from measurements of the reconstructed wavefront over the second telescope's aperture for different heater temperatures. According to the theoretical studies [5], the PSF asymptotically tends to double the phase variance at large separation distances, where the correlation between two points on the wavefront is zero. Figure 4 shows the PSFs and their corresponding double of calculated phase variances for the heater temperatures of 40°C, 80°C, 120°C, and 160°C. As is seen, the values of the PSFs asymptotically tend to these values at large separation distances.

In Fig. 5, some of the experimental data of Fig. 3 and the fitting curves are shown. We have fitted the generalized power-law exponent, Eq. (3), to the experimental data in the range of 0–2.2 cm. For almost all temperatures, the slopes of the structure functions rapidly decrease after this distance. The measured values of the power-law exponent of the fitted lines are shown on the plots. Comparing the fitted power spectrum exponent with the Kolmogorov model, it is seen that the measured PSFs do not obey the power laws associated with the Kolmogorov model.

From the data presented in Fig. 3, it is also easy to investigate that the convective air turbulence is anisotropic turbulence. To

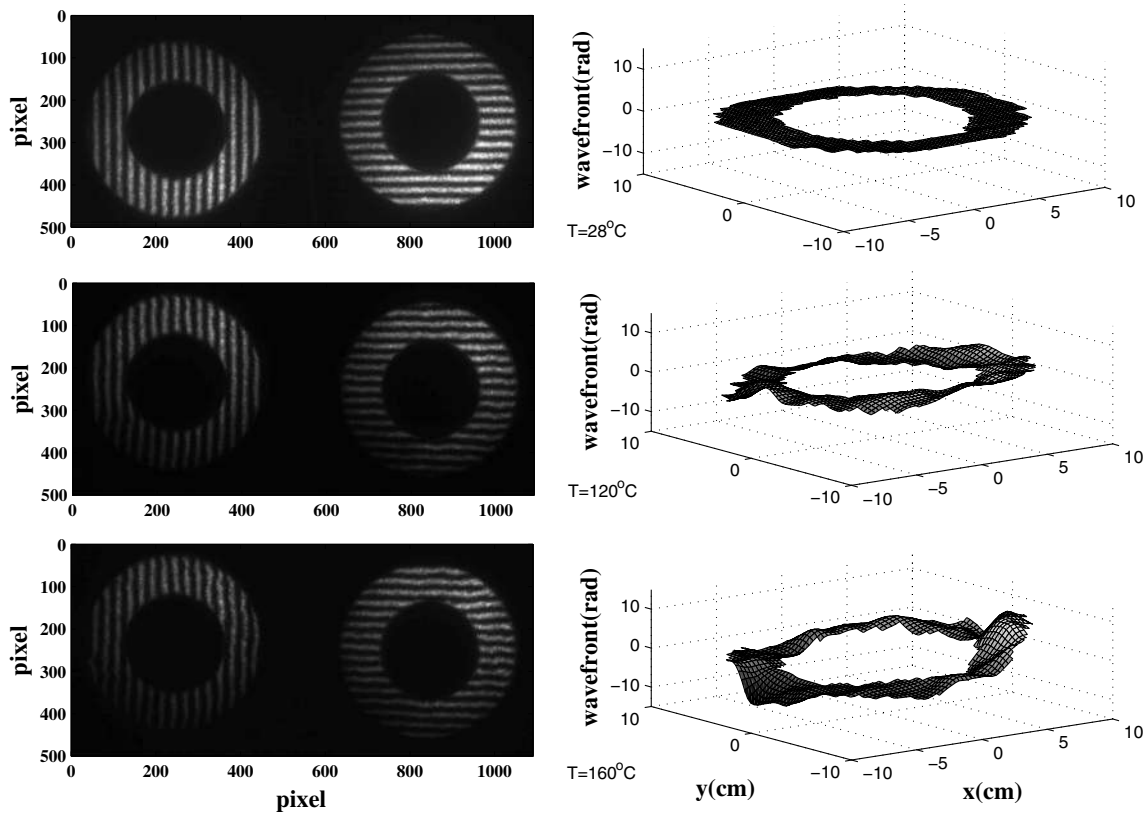

Fig. 2. Three typical recorded frames and corresponding reconstructed wavefronts at three different heater temperatures. The background movie contains 300 corresponding successive frames (Visualization 1).

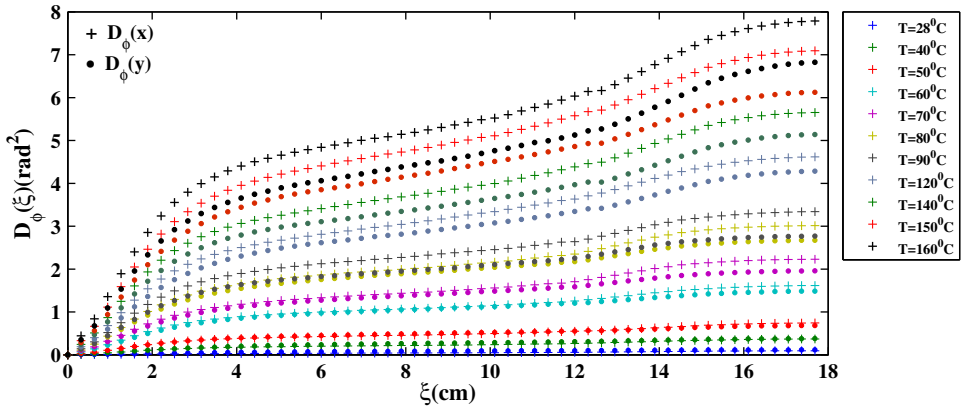

Fig. 3. Calculated PSFs from the reconstructed wavefront over the second telescope's aperture at different heater temperatures for the vertical and horizontal separations.

show the anisotropy of the PSFs in the vertical and horizontal directions, the differences between $D_\phi(x)$ and $D_\phi(y)$ are calculated and plotted in Fig. 6. As is seen, the anisotropy in the statistical properties of the light beam propagating perpendicular to a 2D temperature gradient increases with increasing values of the gradients. In addition, the anisotropy rapidly increases at the smaller separation distances and almost saturates at the higher distances.

We have investigated the correlation between the experimentally obtained data and various other turbulence models:

- The Tatarskii and the Kolmogorov PSF [36]:

$$D_\phi^T(\xi) = 6.88(\xi/r_0)^{5/3}. \tag{6}$$

- The Gaussian PSF [43]:

$$D_\phi^G(\xi) = 0.391 C_n^2 k^2 L \chi_G^{-5/3}\{1 - \exp[-(\xi^2/r_0^2)]\}, \tag{7}$$

where $k = \frac{2\pi}{\lambda}$, $\chi_G = \frac{2\pi}{L_0}$, and L is the propagating beam length. L_0 is the outer scale of turbulence, and λ is wavelength.

- The von Kármán PSF [43]:

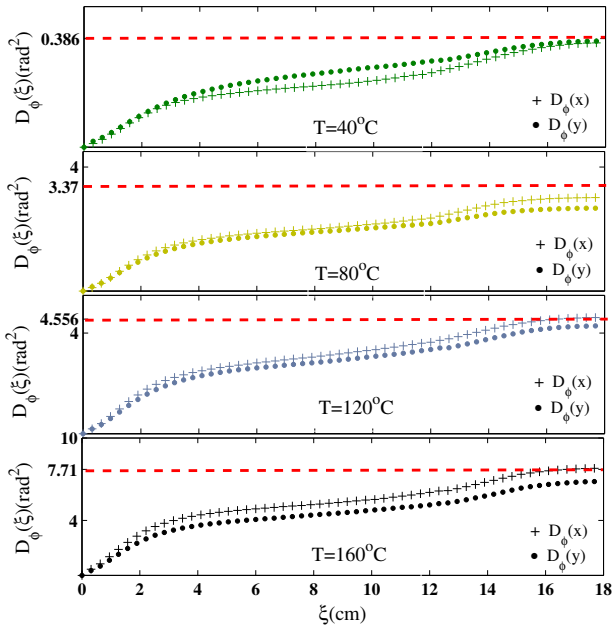

Fig. 4. Calculated PSFs from the reconstructed wavefront over the second telescope's aperture and their corresponding double phase variances at different heater temperatures (the dashed red lines).

$$D_\phi^K(\xi) = 0.391 C_n^2 k^2 L \chi_K^{-5/3} \left[1 - \frac{2^{\frac{1}{6}}}{\Gamma(\frac{5}{6})} (\chi_K \xi)^{\frac{5}{6}} K_{\frac{5}{6}}(\chi_K \xi)\right], \tag{8}$$

where Γ is Gamma function, $\chi_K = \frac{2\pi}{L_0}$, and K is a modified Bessel function of the second kind.

- The Greenwood PSF [44]:

$$D_\phi^{\mathrm{Gr}}(\xi) = 6.88 \left(\frac{\xi}{r_0}\right)^{5/3} {}_2F_3\left(\frac{11}{12}, \frac{17}{12}; \frac{11}{6}, \frac{11}{6}, \frac{1}{2}; -\frac{\xi^2 \chi_{\mathrm{Gr}}^2}{4}\right)$$
$$+32.89(\chi_{\mathrm{Gr}} r_0)^{-5/3} \left[1 - {}_2F_3\left(\frac{1}{12}, \frac{17}{12}; \frac{1}{6}, -\frac{1}{3}, 1; -\frac{\xi^2 \chi_{\mathrm{Gr}}^2}{4}\right)\right]$$
$$-2.27 \xi \chi_{\mathrm{Gr}} \left(\frac{\xi}{r_0}\right)^{5/3} {}_2F_3\left(\frac{17}{12}, \frac{23}{12}; \frac{7}{3}, \frac{7}{3}, \frac{3}{2}; -\frac{\xi^2 \chi_{\mathrm{Gr}}^2}{4}\right), \tag{9}$$

where $\chi_{\mathrm{Gr}} = 3.349/L_0$ and ${}_pF_q$ is the generalized hypergeometric function.

In Fig. 7, different theoretical models are fitted on the experimental PSFs of Fig. 3. The fitted plot can be divided into almost three sections having different slopes. In the fitting process, the Kolmogorov, Gaussian, Greenwood, and von Kármán models were fitted to the experimental data in ranges of 0–2.2 cm,

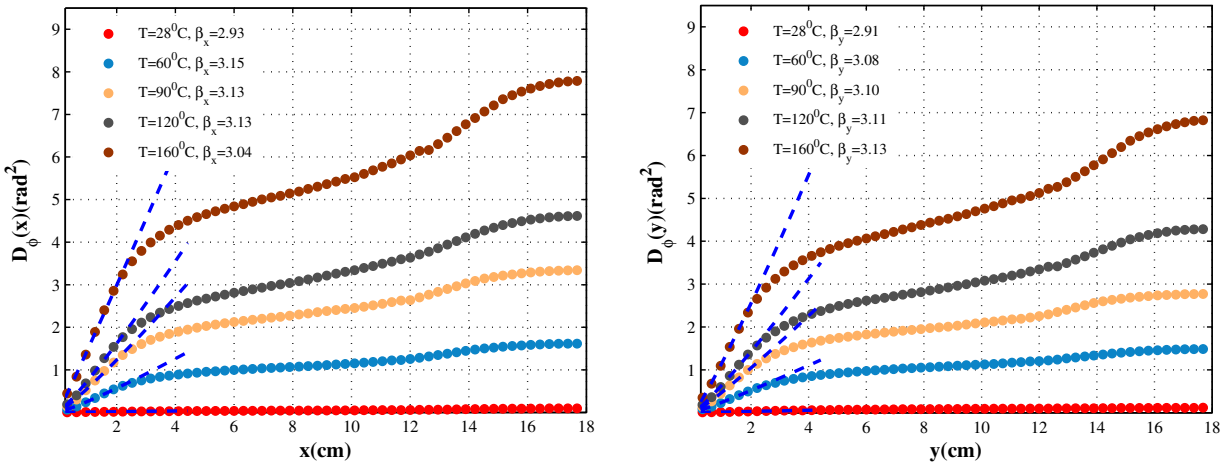

Fig. 5. Calculated power-law exponent of the plots of Fig. 3.

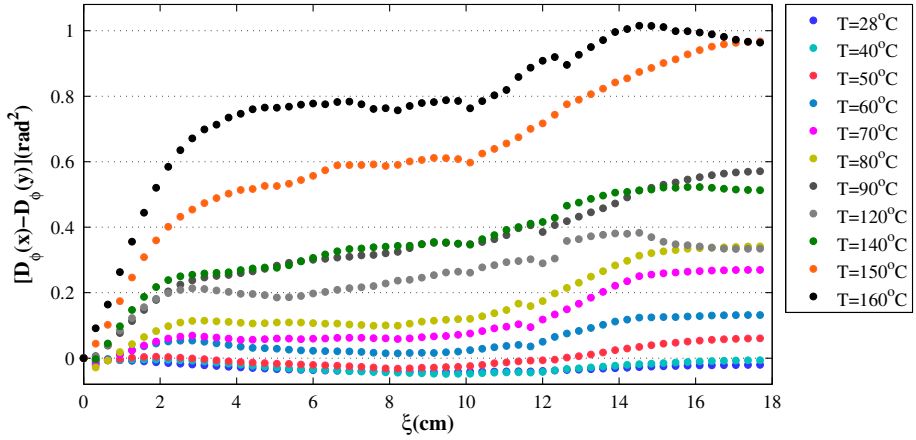

Fig. 6. Difference of the measured PSF in the vertical and horizontal directions for the data presented in Fig. 3.

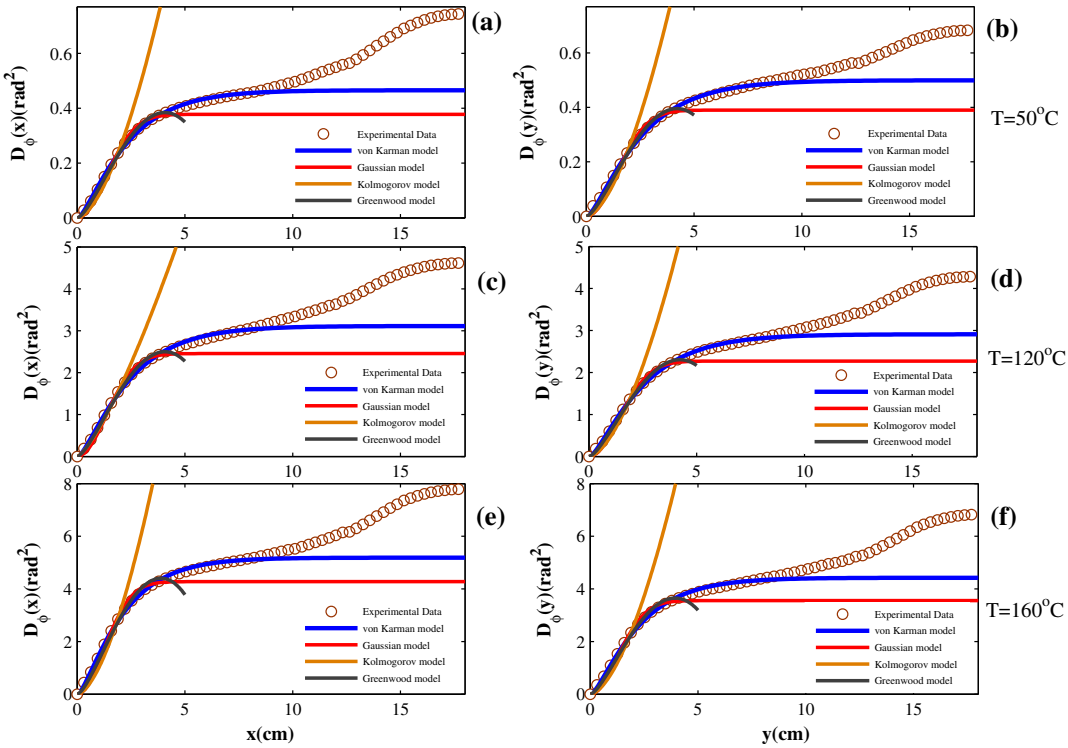

Fig. 7. Experimental PSF and different theoretical models fitted on the experimental data.

Table 2. Mean Square Error of Different Fitted Models

Heater Temperature (°C)	Model	MSE for Fitting $D_\phi(x)$	MSE for Fitting $D_\phi(y)$
40	Kolmogorov	0.0062	0.0058
40	Gaussian	1.8522×10^{-4}	3.1126×10^{-4}
40	von Kármán	5.5161×10^{-6}	5.8435×10^{-5}
40	Greenwood	6.6630×10^{-6}	9.2386×10^{-5}
120	Kolmogorov	0.2627	0.1933
120	Gaussian	0.0085	0.0081
120	von Kármán	0.0038	0.0018
120	Greenwood	0.0032	0.0022
160	Kolmogorov	0.9840	0.6417
160	Gaussian	0.0379	0.0254
160	von Kármán	0.0079	0.0077
160	Greenwood	0.0230	0.0137

0–5 cm, 0–5 cm, and 0–10 cm, respectively. If the models were fitted at greater distances, the mean square error (MSE) of the fittings would significantly be increased. The MSEs of the various models in the mentioned ranges are reported in Table 2. As is seen, the von Kármán model has the best fit to the experimental data because it has the least MSE and is fitted in a larger range than the other models. For the separation values larger than 10 cm, there is no consistency between the experimental data and the existing models.

As has been mentioned above, in Figs. 3–5 and 7, there are three spatial scales in the measured structure functions. Changes in the slopes occur at about 3 and 12 cm, while saturation sets in at about 16 cm. None of the single-scale models—starting with Eq. (6)—are capable of reproducing this complicated behavior. This is demonstrated in Fig. 7, where none of the models provide a reasonable fit to the data at the full 18 cm range. However, as mentioned above, the von Kármán model provides a reasonable fit to the data in the first 10 cm range. Such multi-scale structure functions may arise through the statistical inhomogeneity of the medium and, therefore, can be used for estimation of the size of the volume where the turbulence can be considered as statistically homogeneous. Investigating the physical reasons for such multi-scale structure functions can be the subject of new research efforts.

Values of C_n^2 and the outer scale of the turbulence for different heater temperatures are estimated by fitting the generalized form of the von Kármán PSF,

$$D_\phi^K(u) = a_u\left[1 - \frac{2^{\frac{1}{6}}}{\Gamma(\frac{5}{6})}(\chi_{K_u}u)^{\frac{5}{6}}K_{\frac{5}{6}}(\chi_{K_u}u)\right], \quad u = x, y, \tag{10}$$

to the data of Fig. 3, for the horizontal and vertical separations, respectively. Results are shown in Fig. 8. As is seen, the value of the outer scale decreases for an increase in the temperature of the heater up to approximately 50°C, where it saturates, while the value of C_n^2 monotonically increases.

4. CONCLUSION

In conclusion, this work has illustrated the effect of a 2D temperature gradient on the statistical properties of PSF of a light beam propagating horizontally through an enclosure of convectively turbulent air. The statistical properties of the optical turbulence are investigated through analysis of $D_\phi(x)$ and $D_\phi(y)$ for different temperatures of the heater. Experimental

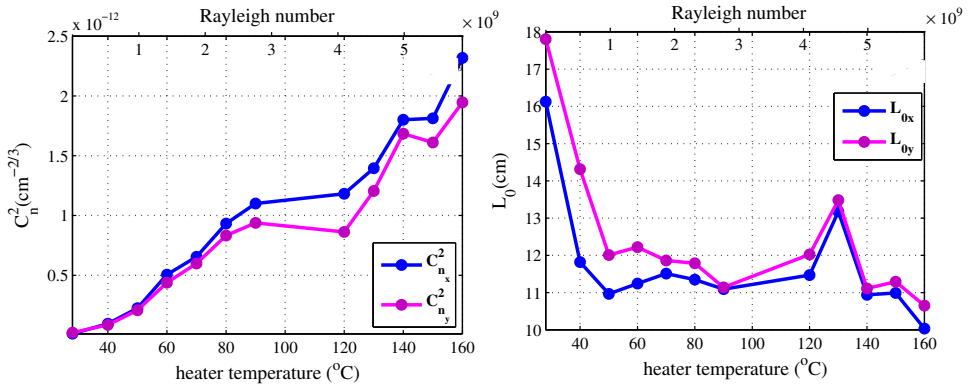

Fig. 8. Estimated values of C_n^2 and the outer scale of the turbulence in different heater temperatures or the corresponding Rayleigh numbers.

results show that the plots of the PSF have three different sections with different slopes. For values of the separation distances inside the first and second sections, the von Kármán PSF is the best fit for the experimental data. By fitting the von Kármán PSF on the data, we estimate values of C_n^2 and the outer scale of the turbulence. Values of the outer scale decreased with increasing temperature of the heater, up to 50°C, after which it was almost saturated. Values of C_n^2 also increased with increasing heater temperatures, albeit without the same saturation.

Finally, we find significant anisotropy for the PSF for increasing temperature gradients and separation distance, and, for values of the latter greater than 10 cm, there is no consistency of the data with any existing model for the PSF.

Funding. Institute for Advanced Studies in Basic Sciences (G2014IASBS12632, G2022IASBS12632).

Acknowledgment. Saifollah Rasouli acknowledges Abdus Salam International Center for Theoretical Physics (ICTP), Trieste, Italy, for Senior Associate Fellowship. We thank M. Dashti for his help during the initial stages of Matlab programming that was needed in this work.

Disclosures. The authors declare no conflicts of interest.

Data availability. The data that support the findings of this study are available upon reasonable request from the authors.

REFERENCES

1. U. Frisch, *Turbulence: the Legacy of A.N. Kolmogorov* (Cambridge University, 1995).
2. J. J. Niemela and K. R. Sreenivasan, "The use of cryogenic helium for classical turbulence: promises and hurdles," J. Low Temp. Phys. **143**, 163–212 (2006).
3. S. Orszag, "Turbulence: challenges for theory and experiment," Phys. Today **43**(1), 24–32 (1990).
4. I. Procaccia and K. R. Sreenivasan, "The state of the art in hydrodynamic turbulence: Past successes and future challenges," Physica D **237**, 2167–2183 (2008) (see page 2170).
5. L. C. Andrews and R. L. Phillips, *Laser Beam Propagation through Random Media* (SPIE, 1998).
6. T. W. Nicholls, G. D. Boreman, and J. C. Dainty, "Use of a Shack–Hartmann wave-front sensor to measure deviations from a Kolmogorov phase spectrum," Opt. Lett. **20**, 2460–2462 (1995).
7. L. C. Andrews, R. L. Phillips, R. Crabbs, and T. Leclerc, "Deep turbulence propagation of a Gaussian-beam wave in anisotropic non-Kolmogorov turbulence," Proc. SPIE **8874**, 887402 (2013).
8. S. Gladysz, K. Stein, E. Sucher, and D. Sprung, "Measuring non-Kolmogorov turbulence," Proc. SPIE **8890**, 889013 (2013).
9. I. Toselli, B. Agrawal, and S. Restaino, "Gaussian beam propagation in maritime atmospheric turbulence: long term beam spread and beam wander analysis," J. Opt. Soc. Am. A **28**, 483–488 (2011).
10. O. Korotkova, "Polarization changes in light beams trespassing anisotropic turbulence," Opt. Lett. **40**, 3077–3080 (2015).
11. S. Rasouli, M. D. Niry, Y. Rajabi, A. A. Panahi, and J. J. Niemela, "Applications of 2-D moiré deflectometry to atmospheric turbulence," J. Appl. Fluid Mech. **7**, 651–657 (2014).
12. M. Dashti and S. Rasouli, "Measurement and statistical analysis of the wavefront distortions induced by atmospheric turbulence using two-channel moiré deflectometry," J. Opt. **14**, 095704 (2012).
13. D. Dayton, B. Pierson, B. Spielbusch, and J. Gonglewski, "Atmospheric structure function measurements with a Shack-Hartmann wave-front sensor," Opt. Lett. **17**, 1737–1739 (1992).
14. V. P. Lukin, "Investigation of anisotropy of the atmospheric turbulence spectrum in the low frequency range," in *International Geoscience and Remote Sensing Symposium* (1996), Vol. **1**, pp. 22–24.
15. L. Biferal and I. Procaccia, "Anisotropy in turbulent flows and in turbulent transport," Phys. Rep. **414**, 43–164 (2005).
16. W. Du, L. Tan, J. Ma, S. Yu, and Y. Jiang, "Measuring of angle of arrival fluctuations over an 11.8 km urban path," Laser Part. Beams **28**, 91–99 (2010).
17. E. Mohammady Razi and S. Rasouli, "Measuring significant inhomogeneity and anisotropy in indoor convective air turbulence in the presence of 2D temperature gradient," J. Opt. **16**, 045705 (2014).
18. S. Rasouli and Y. Rajabi, "Investigation of the inhomogeneity of atmospheric turbulence at day and night times," Opt. Laser Technol. **77**, 40–50 (2016).
19. F. Wang, I. Toselli, J. Li, and O. Korotkova, "Measuring anisotropy ellipse of atmospheric turbulence by intensity correlations of laser light," Opt. Lett. **42**, 1129–1132 (2017).
20. E. M. Razi and S. Rasouli, "Investigation of inhomogeneity and anisotropy in near ground layers of atmospheric air turbulence using image motion monitoring method," Opt. Commun. **383**, 255–259 (2017).
21. M. Beason, C. Smith, J. Coffaro, S. Belichki, J. Spychalsky, F. Titus, R. Crabbs, L. Andrews, and R. Phillips, "Near ground measure and theoretical model of plane wave covariance of intensity in anisotropic turbulence," Opt. Lett. **43**, 2607–2610 (2018).
22. E. M. Razi and S. Rasouli, "Impacts of the source temperature and its distance on the statistical behavior of the convective air turbulence," Appl. Phys. B **125**, 185 (2019).
23. E. M. Razi, S. Rasouli, M. Dashti, and J. J. Niemela, "A high-resolution wavefront sensing method to investigate the annular Zernike polynomials behaviour in the indoor convective air turbulence in the presence of a 2D temperature gradient," J. Mod. Opt. **68**, 994–1001 (2021).
24. V. S. R. Gudimetla, R. B. Holmes, G. Smith, and G. Needham, "Analytical expressions for the log-amplitude correlation function of a plane wave through anisotropic atmospheric refractive turbulence," J. Opt. Soc. Am. A **29**, 832–841 (2012).

25. I. Toselli and O. Korotkova, "General scale-dependent anisotropic turbulence and its impact on free space optical communication system performance," J. Opt. Soc. Am. A **32**, 1017–1025 (2015).
26. M. Yao, I. Toselli, and O. Korotkova, "Propagation of electromagnetic stochastic beams in anisotropic turbulence," Opt. Express **22**, 31608–31619 (2014).
27. X. Xiao, D. G. Voelz, I. Toselli, and O. Korotkova, "Gaussian beam propagation in anisotropic turbulence along horizontal links: theory, simulation and laboratory implementation," Appl. Opt. **55**, 4079–4084 (2016).
28. W. Wanjun, W. Zhensen, S. Qingchao, and B. Lu, "Propagation of Bessel Gaussian beams through non-Kolmogorov turbulence based on Rytov theory," Opt. Express **26**, 21712–21724 (2018).
29. X. Ma, D. Liu, Y. Wang, H. Yin, H. Zhong, and G. Wang, "Propagation of rectangular multi-Gaussian Schell-model array beams through free space and non-Kolmogorov turbulence," Appl. Sci. **10**, 450 (2020).
30. Y. Huang and A. Zeng, "Effect of anisotropic non-Kolmogorov turbulence on the evolution behavior of Gaussian Schell-model vortex beams," Opt. Commun. **436**, 63–68 (2019).
31. M. Bertolotti, M. Carnevale, B. Crosignani, and P. Di Porto, "Influence of thermal turbulence in a convective ascending stream on phase fluctuations of a laser beam," Appl. Opt. **8**, 1111–1114 (1969).
32. V. P. Lukin and V. Pokasov, "Optical wave phase fluctuations," Appl. Opt. **20**, 121–135 (1981).
33. A. Consortini and K. A. O'Donnell, "Beam wandering of thin parallel beams through atmospheric turbulence," Waves Random Complex Medium **1**, S11 (1991).
34. R. V. Shack and B. C. Platt, "Production and use of a lenticular Hartmann screen," J. Opt. Soc. Am. **61**, 656–661 (1971).
35. M. Yeganeh, S. Rasouli, M. Dashti, S. Slussarenko, E. Santamato, and E. Karimi, "Reconstructing the Poynting vector skew angle and wavefront of optical vortex beams via two-channel moiré deflectometery," Opt. Lett. **38**, 887–889 (2013).
36. F. Roddier, *Adaptive Optics in Astronomy* (Cambridge University, 1999).
37. E. Silbaugh, B. Welsh, and M. Roggemann, "Characterization of atmospheric turbulence phase statistics using wave-front slope measurements," J. Opt. Soc. Am. A **13**, 2453–2460 (1996).
38. B. Castaing, G. Gunaratne, F. Heslot, L. Kadanoff, A. Libchaber, S. Thomae, X. Z. Wu, S. Zaleski, and G. Zanetti, "Scaling of hard thermal turbulence in Rayleigh-Bénard convection," J. Fluid Mech. **204**, 1–30 (1989).
39. S. Rasouli, M. Dashti, and A. N. Ramaprakash, "An adjustable, high sensitivity, wide dynamic range two channel wave-front sensor based on moiré deflectometry," Opt. Express **18**, 23906–23915 (2010).
40. W. H. Southwell, "Wave-front estimation from wave-front slope measurements," J. Opt. Soc. Am. **70**, 998–1006 (1980).
41. M. Dashti and S. Rasouli, "Implementation of a wavefront-sensing algorithm with two-channel moiré deflectometry and Matlab graphic user interface," Optoelectron. Instrum. Data Process. **57**, 683–694 (2021).
42. M. H. Daemi and S. Rasouli, "Investigating the dynamic behavior of thermal distortions of the wavefront in a high-power thin-disk laser using the moiré technique," Opt. Lett. **45**, 4567–4570 (2020).
43. A. Consortini and L. Ronchi, "Choice of the model of atmospheric turbulence," Appl. Opt. **11**, 1205–1211 (1972).
44. V. V. Voitsekhovich, "Outer scale of turbulence: comparison of different models," J. Opt. Soc. Am. A **12**, 1346–1353 (1995).